Nuclear Instruments and Methods in Physics Research A 772 (2015) 43–49

Contents lists available at ScienceDirect

Nuclear Instruments and Methods in Physics Research A

journal homepage: www.elsevier.com/locate/nima

Digital neutron/gamma discrimination with an organic scintillator at energies between 1 MeV and 100 MeV

A.C. Comrie [a], A. Buffler [a,*], F.D. Smit [b], H.J. Wörtche [c]

[a] Department of Physics, University of Cape Town, Rondebosch 7700, South Africa
[b] iThemba LABS, Somerset West 7129, South Africa
[c] INCAS[3], Dr. Nassaulaan 9. 9400 AT Assen, The Netherlands

ARTICLE INFO

Article history:
Received 26 May 2014
Received in revised form
29 August 2014
Accepted 26 October 2014
Available online 4 November 2014

Keywords:
Liquid scintillator
Neutron detection
Digital pulse shape discrimination

ABSTRACT

Three different digital implementations of pulse shape discrimination for pulses from an EJ301 liquid scintillator detector are presented, and illustrated with neutrons and gamma-rays produced by an Am–Be radioisotopic source, a D–T generator and beams produced by cyclotron-accelerated protons of energies 42, 62 and 100 MeV on a Li target. A critical comparison between the three methods is provided.

1. Introduction

The development of methods to detect neutrons, both thermal and fast, has enjoyed significant resurgence in recent years, mainly due to the demands of security applications [1]. Although a number of novel techniques have emerged [2,3], most approaches still rely on the physical mechanisms offered by the detection of charged particles recoiling from neutron-induced interactions, such as n–p elastic scattering or fast fission, which is used as a metrology standard [4]. When reasonable efficiency or fast timing is required, the hydrocarbon-based scintillator remains the detector of choice for spectroscopic measurements of fast neutrons. Since the radiation fields of fast neutrons nearly always also include gamma-rays, techniques for distinguishing between the signals associated with fast neutrons and gamma-rays need to be employed. The light output of these scintillators displays both fast and slow decay components [5], and the proportion of these is related to the specific energy loss of the recoiling charged particle by the Birks relation [6].

Pulse shape discrimination (PSD), established in the 1950s [7] and developed through the 1960s [5], allows the identification of different types of charged particles in certain scintillator detectors by means of the characteristics of the scintillation decay. Liquid organic scintillators such as the nearly equivalent NE213, BC501A and EJ301 persist as popular detector types for this application. Two approaches to PSD have dominated. One technique employs the differences in the rise times of the pulses associated with different recoiling charged particles in the scintillator (the "zero crossing" method [8]), and the other, the difference between the integrals of these pulses over a few nanoseconds following the leading edge (the "charge comparison" method, most notably implemented in the "LINK" module [9]). The implementation of these techniques with analogue electronics has often posed challenges with respect to quality and reliability when PSD has been employed in field applications.

Two recent technological developments are assisting the employment of hydrocarbon-based detectors together with PSD in non-laboratory environments. Firstly, the development of solid (plastic) polyvinyltoluene-based detectors [10–12] which exhibit PSD capability removes the toxic and fire hazards associated with most liquid scintillators. Secondly, the emergence of digital data acquisition and processing systems allows a number of flexible pulse shape discrimination algorithms to be implemented and dynamically optimised in software form [13–15].

We present and compare the application of three software-implemented algorithms for the analysis of the shapes of digitally stored pulses from a liquid scintillator when exposed to a range of mixed neutron–gamma radiation fields, spanning neutron energies between 1 and 100 MeV. The implementation of the same algorithm for PSD across a wide energy range is a necessary prerequisite for the application of digital PSD in a detector system which may be employed to measure secondary neutrons from cosmic ray interactions or at accelerator facilities, for example, where the energy spectrum features prominent enhancements both at low energy and around 100 MeV [16].

* Corresponding author. Tel.: +27 21 650 3339.
E-mail address: andy.buffler@uct.ac.za (A. Buffler).

http://dx.doi.org/10.1016/j.nima.2014.10.058
0168-9002/

2. Experimental setup

The detector used for the measurements consisted of an encapsulated EJ301 liquid scintillator (51 mm diameter × 51 mm) optically coupled to an ETL 9214 12-stage photomultiplier tube and base, supplied by Scionix, and operated at a negative bias of 950 V. Signals from the PMT anode were digitised by a CAEN Vx1761 2-channel 10 bit digitiser, operating at 4 GS/s with a peak-to-peak range of 1 V. Custom-built software was used to record data for offline analyses.

Neutrons and gamma-rays were provided via three methods: a 2 GBq ^{241}Am–^{9}Be (Am–Be) radioisotopic source, a Thermo Scientific MP320 ^{2}H–^{3}He (D–T) neutron generator and proton beams produced at the cyclotron facility of iThemba LABS, South Africa. The Am–Be source produces 4.43 MeV gamma-rays and neutrons having a complex energy spectrum with a maximum energy of about 10 MeV, and was used in open geometry. The D–T generator produces neutrons of nominal energy 14 MeV via the ^{3}He(d,n)^{4}He reaction at a rate of about 10^{8} per second, and was housed in a $3 \times 3 \times 2$ m^3 cave constructed from polyethylene bricks.

The k=200 Separated-Sector Cyclotron (SSC) of the iThemba LABS accelerates protons in the energy range from 20 MeV to 200 MeV. A beam pulse selector can suppress a chosen fraction of proton bunches to enlarge the time interval between pulses, which allows time of flight (ToF) measurements to be carried out [17]. Typical currents for 100 MeV are about 5 mA in unselected mode and 500 nA at the repetition rate of 2.5 MHz. The ^{7}Li(p, n)^{7}Be reaction was employed to produce quasi-monoenergetic neutron beams, since this reaction proceeds only by the transition to the ground state and the first excited state of ^{7}Be, with all higher levels being unstable. A quasi-monoenergetic neutron emission, which is strongly forward peaked, is obtained in this way [17]. A 2 m thick steel collimator with openings at 0° and 16° shapes 8 × 8 cm^2 beams at 6 m. The collimator is lined on the outside by a layer of borated wax and polyethylene. Background measurements were carried out by bombarding an empty position of the target ladder at the same focusing employed for the measurements. A cleaning magnet deflects proton beams into the well shielded beam stop, where a Faraday cup measures the beam current. In the present work, proton energies of 42, 62 and 100 MeV were used, and the detector was mounted coaxially at 6 m from the target for each run. A 3 mm natural Li target was used for the 42 MeV beam, while an 8 mm Li target was used for the 62 MeV and 100 MeV beams.

3. Pulse shape discrimination by charge comparison

Fig. 1(a) shows typical digitised pulses, both chosen to have the same total integral, but associated with the interactions of a neutron and a gamma-ray in the detector, produced during a run with the D–T generator. The corresponding cumulative integrals of these pulses are shown in Fig. 1(b). The baseline, calculated as an average of 300 samples preceding the leading edge of each pulse, was subtracted to avoid effects of voltage drift. The PMT voltage was chosen to ensure that the signals peaked between 50 mV and 900 mV in order to avoid voltage saturation of the digitiser. Pulses associated with gamma-rays and neutrons typically drop to 1% of their peak value after 100 and 150 ns respectively. Statistical fluctuations associated with the finite number of photons produced in the scintillator and the limited efficiency of the PMT are responsible for variations in the pulse shapes, while the uncertainty introduced by digitisation is below 1 mV.

A consistent signal start time t_0 was defined in a way which minimised effects due to variations in pulse noise, baseline, amplitude and shape. A software-implemented digital constant fraction discriminator (dCFD) filter was applied to each signal. The

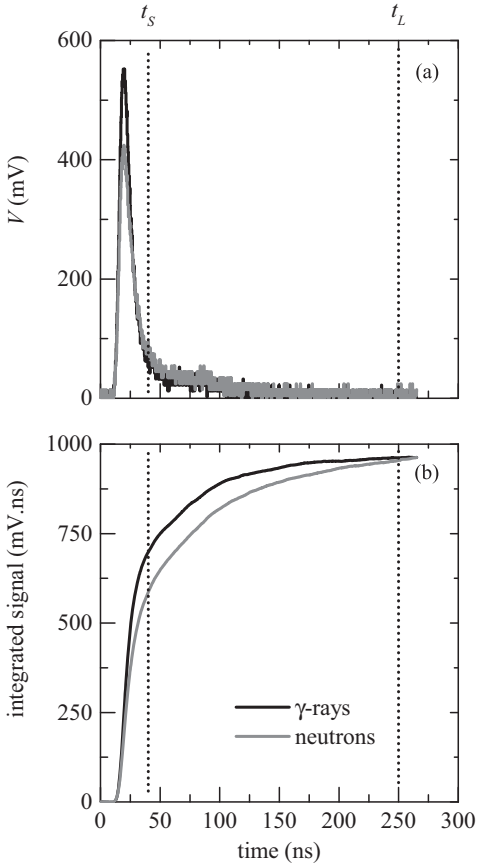

Fig. 1. Typical digitised (a) pulses and (b) pulse integrals for events arising from neutron and gamma-ray interactions in the EJ301 scintillator. The pulses were selected to have the same total integral and are shown after baseline subtraction. Integration times t_S and t_L are indicated.

filtered signal v takes the form of

$$v_i = \sum_{j=1}^{N} fV_{i-j} - V_{i-j-D} \quad (1)$$

where V is the unfiltered signal, N is the filter length, D is the filter offset and f is the filter fraction [18]. The values of these parameters were chosen to optimise the time resolution of the acquisition system, which was determined by splitting a test signal across two digitiser channels and calculating the FWHM of the distribution of differences between signal start times. Typical FWHMs of 40 ps were calculated, well below the sampling interval of 250 ps.

Fig. 2 shows an example of a digitised pulse after application of the dCFD filter. A linear fit to 5 samples in the region of the pulse indicated by the dotted lines in Fig. 2 was used to determine the time of intersection of the filtered signal with the baseline (dashed line). The time t_0 was then determined as the time of this intersection minus a constant offset of 25 ns, in order to include the entire pulse in further calculations.

For each recorded event, a parameter Q_L was calculated by integrating the digitised signal over a 250 ns time interval (t_L), starting from t_0. The gamma-rays from ^{22}Na, ^{137}Cs, ^{207}Bi and Am–Be radioisotopic sources were used for scaling Q_L to a light output parameter L in units of MeV electron equivalent (MeV$_{ee}$). The relationship between Q_L and L was found to be linear over the energy range of the calibration sources, and was assumed to be linear over the energy range of the measurements. The value of t_L was chosen in order to capture as much of the entire signal as possible, while still avoiding saturation of the available output transfer rate of the digitiser. A

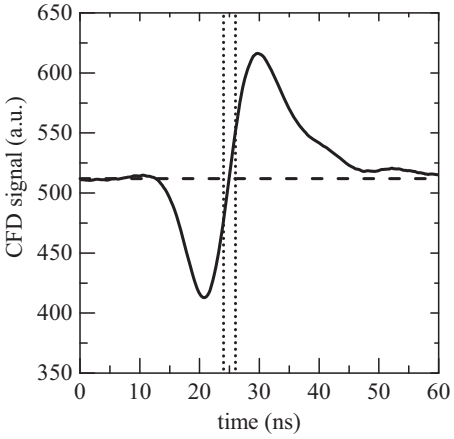

Fig. 2. Typical digitised pulse after application of the dCFD filter. The dotted lines indicate the region used to determine the time of intersection of the filtered signal with the baseline (dashed line).

second parameter Q_S was calculated by integrating the pulse over a shorter time interval (t_S). A pulse shape parameter S was then defined as

$$S = k\frac{Q_S}{Q_L} + C \tag{2}$$

which is the basis of a charge comparison method of PSD. Constants k and C were chosen in order to appropriately scale and offset S. Signals arising from gamma-ray interactions with the detector have a reduced slow decay component in comparison to those arising from neutron interactions. Therefore, a larger proportion of light output occurs within the shorter time interval in gamma-ray events, leading to higher values of S when compared to neutron events of a similar light output. Statistical fluctuations in pulse shape lead to Gaussian distributions of S for gamma-ray and neutron events with equal values of Q_L.

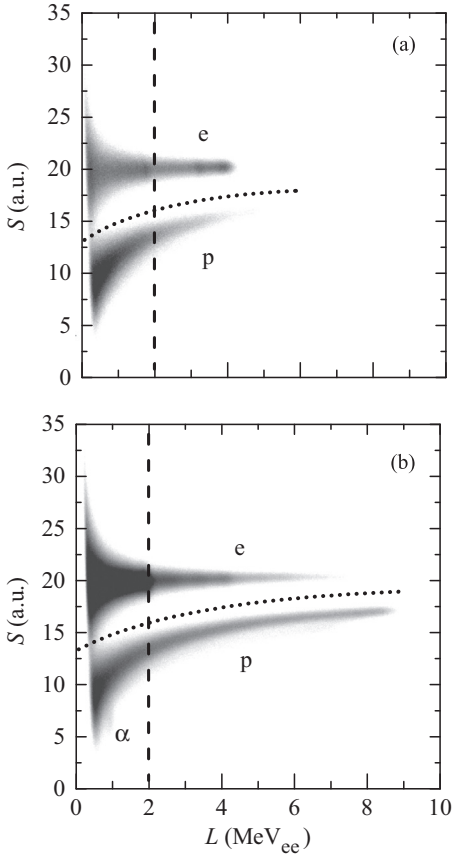

Fig. 3. Counts as a function of light output parameter L and pulse shape parameter S for events in the scintillator when exposed to neutrons and gamma-rays from (a) the Am–Be source and (b) the D–T generator. Loci associated with recoiling electrons (e), protons (p) and alpha-particles (α) are indicated. The dotted lines indicate the cuts used to separate neutron and gamma-ray events and the dashed lines the cut used to select events in the range $L = 1.9$–2.1 MeV$_{ee}$.

3.1. Measurements using the Am–Be source and D–T generator

Fig. 3 shows distributions of events as a function of parameters L and S for two typical runs with (a) the Am–Be source and (b) the D–T generator. The loci associated with recoiling electrons from Compton scattering events (gamma-rays) and protons recoiling from n–p elastic scattering (neutrons) are well separated over the full range of L. Also evident in Fig. 3(b) is a small locus associated with alpha-particles emitted from neutron interactions with the ^{12}C in the scintillator. The gamma-ray events result mainly from the detection of (a) 4.43 MeV gamma rays from the de-excitation of ^{12}C in the Am–Be source and (b) 4.43 MeV and 2.23 MeV gamma-rays produced respectively by ^{12}C(n,n′) and ^{1}H(n,γ)d interactions in the polyethylene (C_nH_{2n}) blocks forming the cave. The "soft" slanted threshold at low L is a result of the dependence of the trigger of the digitiser module on the signal height, rather than the magnitude of Q_L. This leads to a lower threshold for gamma-ray events since these pulses have a shorter decay time. The dotted lines show cuts to separate events associated with neutrons and gamma-rays. The projections of these selections onto the L-axis are shown in Fig. 4. The dashed lines in Fig. 3 indicate a cut to select events in the range $L = 1.9$–2.1 MeV$_{ee}$, which are projected onto the S-axis in Fig. 5.

A figure of merit (FoM) is a useful means to provide a quantitative measurement of the separation between the distributions of S for two pulse classes [19]. If these distributions are Gaussian in form, it is reasonable to define a FoM in terms of the mean μ and full width at half maximum (FWHM) of the two distributions:

$$\mathrm{FoM} = \frac{|\mu_e - \mu_p|}{FWHM_e + FWHM_p} \tag{3}$$

The FoM for the distributions shown in Fig. 5 is 2.2. Short integration time t_S was chosen in order to optimise the FoM, with a typical value of 35 ns.

3.2. Measurements using 42, 62 and 100 MeV proton beams

At energies above ~20 MeV, neutron interactions with ^{12}C nuclei in the scintillator become more important relative to n–p elastic scattering. In addition, the relative proportion of charged particles which escape from the scintillator before depositing all of their energy increases with increasing incident neutron energy.

Pulsed beams of quasi-monoenergetic neutrons were produced via the ^{7}Li(p,n)^{7}Be reaction by proton beams of energy 42, 62 or 100 MeV from the $k = 200$ cyclotron of iThemba LABS [17]. Measurements were made at 0° at a distance 6.00 m from the target. A time-of-flight parameter T was determined as the difference between t_0 for the detector event pulse and t_0 determined for a reference pulse associated with the preceding proton beam bunch, provided by the pulse selector of the cyclotron and digitised in a separate channel. Fig. 6 shows the distribution of events as a function of L and T measured for a run with the 62 MeV proton beam. The distribution of neutron-induced events at $T = 132$ ns is dominated by direct production of neutrons via the unresolved (ground state + 0.429 MeV) transition of the ^{7}Li(p,n)^{7}Be reaction,

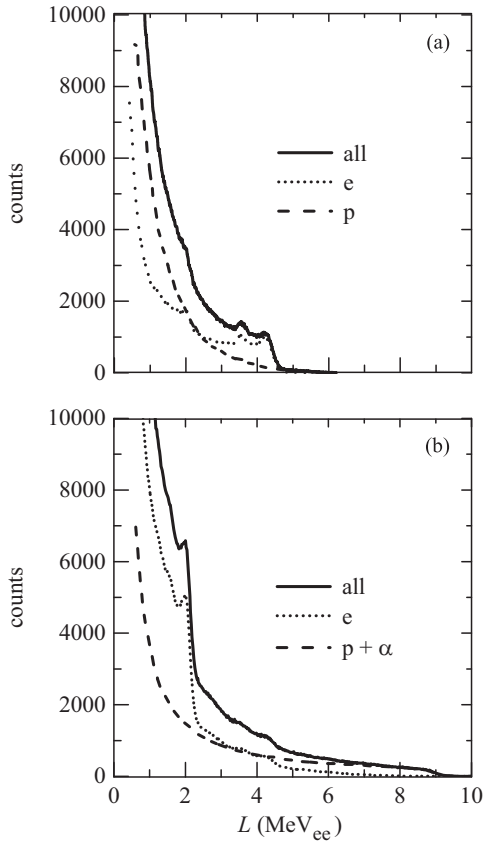

Fig. 4. Light output L spectra for events from runs with (a) the Am–Be source and (b) the D–T generator, as selected by the cuts in Fig. 3.

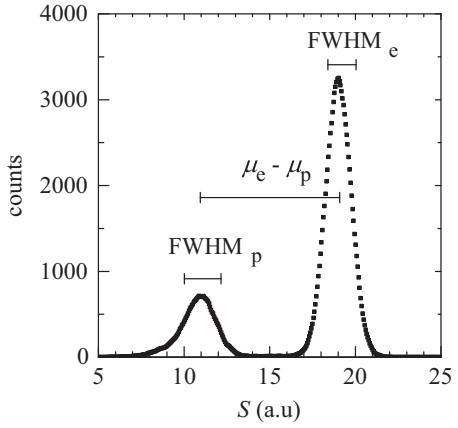

Fig. 5. Counts versus shape parameter S for events in the range of $L=1.9$–2.1 MeV_{ee} from a run with the D–T generator.

which is strongly forward peaked in the laboratory frame [20]. The continuum evident between $T=135$ ns and 350 ns is associated with isotropic breakup reactions. The sharp peak at $T=91$ ns (FWHM 0.70 ns) is associated with gamma-rays produced in the Li target, and the uniform time-independent distribution of gamma-rays is associated with background in the experiment hall.

Fig. 7 shows distributions of events as a function of L and S produced for runs with proton beams of energy (a) 42 MeV, (b) 62 MeV and (c) 100 MeV. Loci attributed to different charged particles released by n–p elastic scattering or by n–C interactions in the scintillator are identified as follows in Fig. 7(b): protons (p); deuterons (d); tritons (t) and alpha-particles (α). Events in the region between loci t and α can be attributed to ^{3}He ions, or to the

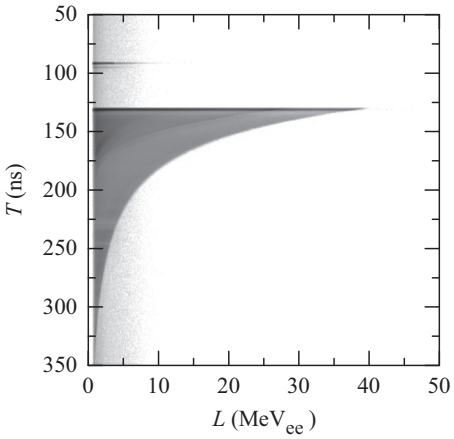

Fig. 6. Counts as a function of light output parameter L and time-of-flight parameter T from measurements made using a 62 MeV proton beam irradiating an 8 mm Li target, at a distance of 6.00 m from the target at 0°.

simultaneous detection of two or more charged particles. A locus (e) is associated with recoiling electrons (gamma-ray events), and locus (ep) with charged particles (mainly protons) which escape from the 5.1 cm long detector. The ep and e loci merge at lower L, since escaping charged particles do not deposit their Bragg peak, resulting in a significant reduction in the proportion of Q_L to Q_S. The higher proportion of escaping protons is clearly evident at 100 MeV (Fig. 7(c)), where the range of a 100 MeV proton in EJ301 is 8.7 cm. The dotted line indicates the cut used to exclude events associated with gamma-rays. The dashed lines in Fig. 7(b) indicate a cut selecting events in the range $L=19$–21 MeV_{ee}, which are projected onto the S-axis in Fig. 8. The distributions for protons, deuterons, tritons and escaping protons are easily discernable. Fig. 9 shows light output, L, spectra for the three energies, after gamma-ray events were excluded, together with the spectral components associated with the recoil of protons, deuterons and alpha-particles, selected by PSD (Fig. 7).

Neutron energy spectra were determined from the time-of-flight measurements, and are shown in Fig. 10 normalised to unity, after correcting the measurements for the efficiency of the detector. The spectra agree within 5% of previous measurements at iThemba LABS using traditional analogue electronics [21]. The width of the quasi-monoenergetic neutron peak is dominated by contributions from the energy loss of the proton beam in the Li target and the intrinsic time resolution of the scintillator, and not the timing resolution of the digital data acquisition system.

3.3. Pulse shape discrimination by zero-crossing and linear filter methods

In addition to the charge comparison approach illustrated above, methods based on zero-crossing timing and the application of a linear filter were also implemented on the same data sets.

3.3.1. Zero-crossing PSD

The zero-crossing algorithm uses a combination of filters to shape integrated pulses into a bipolar signal, and determines the time at which the signal switches polarity. This “zero-crossing” of the bipolar signal will be dependent on the rise time of the integrated pulse, and can therefore be used to classify pulses. This method has been shown to outperform the digital charge comparison algorithm under certain conditions [22].

An alternative implementation of the zero-crossing algorithm, utilised in this work, evaluates the rise time of the cumulative integral of the signal, without a pulse shaping network [23]. The

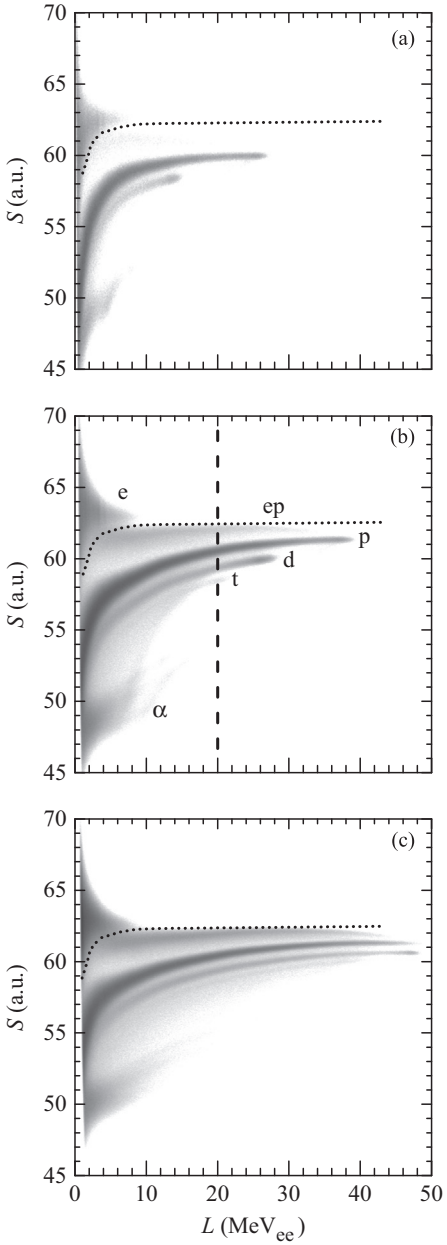

Fig. 7. Counts as a function of light output parameter L and pulse shape parameter S for events in the scintillator when exposed to neutrons and gamma-rays produced by the irradiation of a Li target by proton beams of energy (a) 42 MeV, (b) 62 MeV and (c) 100 MeV. Loci associated with recoiling electrons (e), protons (p), escaping protons (ep), deuterons (d), tritons (t) and alpha-particles (α) are indicated. The dotted lines indicate the cuts used to separate neutron and gamma-ray events and the dashed lines the cut used to select events in the range $L=19$ to 21 MeV$_{ee}$.

evaluation of the rise time is performed by determining the difference between the times at which the integrated signal crosses low and high thresholds. Thresholds were chosen in order to optimise the FoM, with typical values of 15% and 65% of Q_L for low and high thresholds, respectively.

3.3.2. *Linear filter PSD*

The linear filter algorithm is a generalised implementation of the charge comparison method. In this approach, the shape parameter S is defined by

$$S=\sum P_i V_i \tag{4}$$

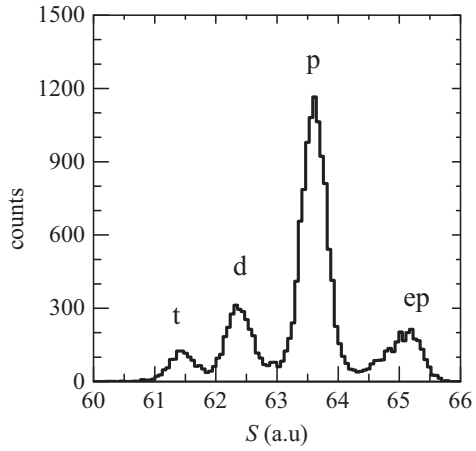

Fig. 8. Counts versus shape parameter S for events in the range of $L=19$–21 MeV$_{ee}$ from a run with the 62 MeV proton beam. The labels indicate event distributions associated with recoiling protons (p), deuterons (d) and tritons (t), and protons which escape from the detector (ep) before depositing all of their energy.

where V is the digitised signal and P is a weighting vector with the same number of samples as the digitised signal. For the case of charge comparison, P is a step function with a value of unity within the short time interval and zero elsewhere. Theoretical calculations show that the optimal weights which maximise the FoM under ideal conditions are

$$P_i=\frac{W_{Ni}-W_{\gamma i}}{W_{Ni}+W_{\gamma i}} \tag{5}$$

where W_{Ni} and $W_{\gamma i}$ are the digitised samples of the average pulse shapes from neutron and gamma-ray events respectively [24].

The use of a genetic algorithm to determine optimal weights by performing a non-exhaustive search through all possible forms of P has been previously demonstrated [25] and was implemented. Rather than optimising P directly, a shortened weighting vector was optimised and then interpolated to determine P. The reduction of the vector length enables a significantly shorter computation time. It was found that increasing the number of weights above 100 did not improve results noticeably.

4. Discussion

The charge comparison, zero-crossing and linear filter algorithms were compared by calculating FoMs over a wide range of L from data measured using the D–T generator (Fig. 3(b)) and the 62 MeV proton beam (where the FoM was determined using the proton and deuteron loci, see Fig. 7(b)). Fig. 11 shows FoM as a function of L for each algorithm for the D–T generator data. The FoMs from all three algorithms follow a similar trend, with FoM improving and converging with increasing L. This is primarily due to the improved signal-to-noise ratio as the number of photoelectrons increases with L. At low L, the linear filter algorithm produces a better FoM over the other two approaches. Fig. 12 shows FoM as a function of L for the 62 MeV proton beam data The FoMs follow very similar trends, with the zero-crossing method consistently producing the smallest FoM. Separation between the proton and deuteron loci improves with increasing L as expected. However, the FoM values for the p–d data are consistently lower than those for the p–e data derived from the D–T generator measurements, as governed by the specific light output functions for electrons and much heavier charged particles, which produce less distinctive responses.

One of the primary advantages of utilizing a digital acquisition system for PSD is the ability to perform offline analyses, in order to optimise PSD parameters that would otherwise be fixed at the

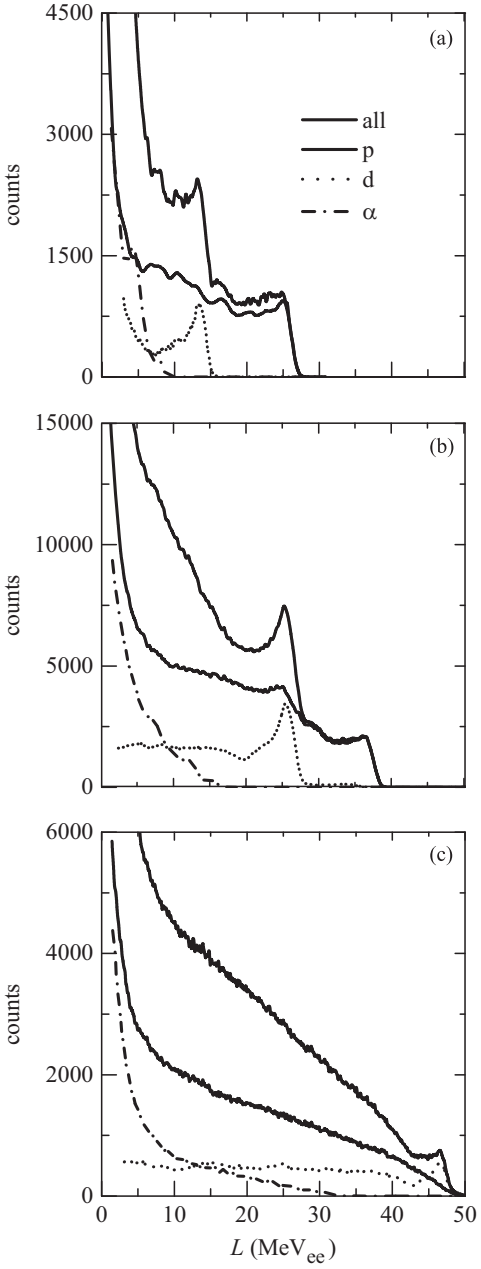

Fig. 9. Light output L spectra for events from runs with the proton beams, with components associated with the recoil of protons, deuterons and alpha-particles, selected by PSD. (a)EP = 42 MeV, (b) EP = 62 MeV and (c) EP = 100 MeV.

time of the experiment. Fig. 13 shows FoM as a function of t_S for the charge comparison algorithm, measuring p–e discrimination at $L=2$ MeV$_{ee}$ and p–e discrimination at $L=20$ MeV$_{ee}$ (see Figs. 3(b) and 7(b) respectively). For measurements with the D–T generator (and similarly for the AmBe source) the optimal value of t_S is around 40 ns, while for p–d discrimination at higher L it is seen that t_S should be 10 ns longer.

5. Conclusion

Three different digital implementations of pulse shape discrimination in an EJ301 liquid scintillator detector have been presented, and illustrated with neutrons and gamma-rays produced by an Am–Be radioisotopic source, a D–T generator and beams produced by cyclotron-accelerated protons of energies 42, 62 and 100 MeV.

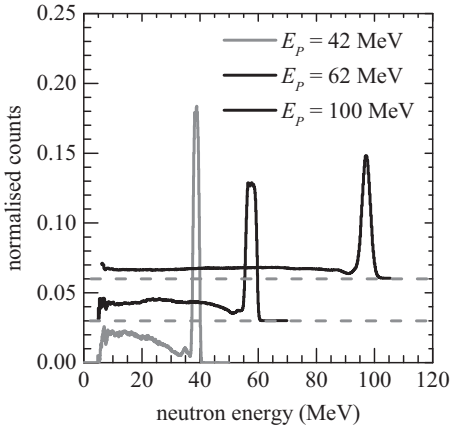

Fig. 10. Neutron energy spectra determined via time-of-flight for runs with proton beams of energies of 42, 62 and 100 MeV irradiating a lithium target. The spectra have been normalised to unity after being corrected for detector efficiency.

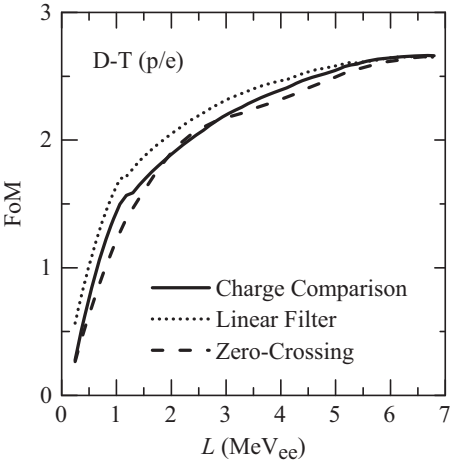

Fig. 11. Figure of merit versus L for events from a run with the D–T generator, showing neutron/gamma-ray separation.

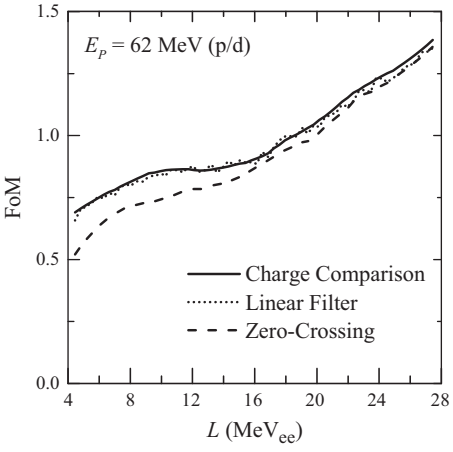

Fig. 12. Figure of merit versus L for events from a run with the 62 MeV$_{ee}$ proton beam, showing proton/deuteron separation.

We have shown that the same implementations of the three algorithms can be used in PSD systems dealing with a wide range of neutron energies (1–100 MeV). All three methods produce similar quality of PSD to digital methods previously presented [23,25,12] and have been shown for the first time to produce PSD at higher energies of a quality similar to the state-of-the-art in

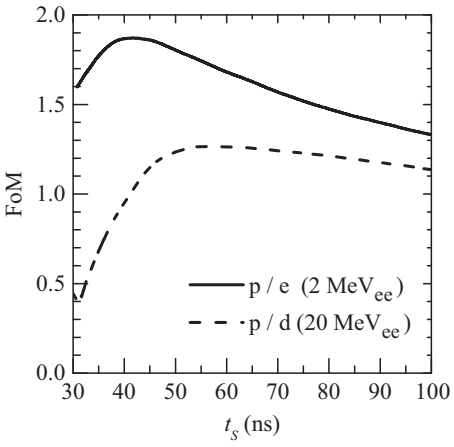

Fig. 13. Figure of merit versus t_S, for events from runs with the D–T generator (neutron/gamma-ray separation in the range $L=1.9$–2.1 MeV$_{ee}$) and the 62 MeV proton beam (proton/deuteron separation in the range $L=19$–21 MeV$_{ee}$).

analogue implementation of PSD [26]. Neutron energy spectra derived from these data (Fig. 10) are also comparable with previous measurements made with conventional NIM-type electronics at neutron energies between 5 and 100 MeV[21].

The charge comparison method, as implemented, produces the best quality PSD at higher energies and is not improved significantly by the inclusion of a weighted integration algorithm. The zero-crossing method appears to produce consistently poorer results across the entire range of L. A notable advantage of digital PSD is that optimisation of critical parameters such as t_S can occur after the data are recorded. This is particularly significant for experiments spanning a wide energy range: since the optimal value of t_S has been shown to vary with L, t_S can be chosen as a function of L to produce the best FoM across the full range of L.

Acknowledgements

We thank the staff of iThemba LABS for their help in carrying out the experiments, the staff of the UCT Physics Department workshop for constructing equipment used and the National Research Foundation (South Africa) for financial support.

References

[1] A. Buffler, J. Tickner, Radiation Measurements 45 (10) (2010) 1186.
[2] F.D. Brooks, H. Klein, Nuclear Instruments and Methods in Physics Research Section A 476 (1) (2002) 1.
[3] D.J. Thomas, Radiation Measurements 45 (10) (2010) 1178.
[4] D.J. Thomas, R. Nolte, V. Gressier, Metrologia 48 (6) (2011) S225.
[5] F.D. Brooks, Nuclear Instruments and Methods 162 (1) (1979) 477.
[6] J.B. Birks, Proceedings of the Physical Society Section A 64 (10) (1951) 874.
[7] G.T. Wright, Proceedings of the Physical Society Section B 69 (3) (1956) 358.
[8] M.L. Roush, M.A. Wilson, W.F. Hornyak, Nuclear Instruments and Methods 31 (1) (1964) 112.
[9] J.M. Adams, G. White, Nuclear Instruments and Methods 156 (3) (1978) 459.
[10] N. Zaitseva, B.L. Rupert, I. Pawełczak, A. Glenn, H.P. Martinez, L. Carman, M. Faust, N. Cherepy, S. Payne, Nuclear Instruments and Methods in Physics Research Section A 668 (2012) 88.
[11] S.A. Pozzi, M.M. Bourne, S.D. Clarke, Nuclear Instruments and Methods in Physics Research Section A 723 (2013) 19.
[12] D. Cester, G. Nebbia, L. Stevanato, F. Pino, G. Viesti, Nuclear Instruments and Methods in Physics Research Section A 735 (2014) 202.
[13] B. Esposito, Y. Kaschuck, A. Rizzo, L. Bertalot, A. Pensa, Nuclear Instruments and Methods in Physics Research Section A 518 (1) (2004) 626.
[14] Y. Kaschuck, B. Esposito, Nuclear Instruments and Methods in Physics Research Section A 551 (2) (2005) 420.
[15] K.A.A. Gamage, M.J. Joyce, N.P. Hawkes, Nuclear Instruments and Methods in Physics Research Section A 642 (1) (2011) 78.
[16] M. Takada, K. Yajima, H. Yasuda, T. Sato, T. Nakamura, Journal of Nuclear Science and Technology 47 (10) (2010) 932.
[17] M. Mosconi, E. Musonza, A. Buffler, R. Nolte, S. Röttger, F.D. Smit, Radiation Measurements 45 (10) (2010) 1342.
[18] H. Peng, P.D. Olcott, A.M.K. Foudray, C.S. Levin, Evaluation of free-running adcs for high resolution pet data acquisition, in: IEEE Nuclear Science Symposium Conference Record, 2007. NSS'07, vol. 5, IEEE, 2007, p. 3328, ⟨http://ieeexplore.ieee.org/xpls/abs_all.jsp?arnumber=4436846⟩.
[19] C.E. Brient, C.E. Nelson, R.L. Young, Nuclear Instruments and Methods 98 (2) (1972) 329.
[20] H. Hideki, R. Nolte, Metrologia 48 (6) (2011) S292.
[21] R. Nolte, M.S. Allie, R. Böttger, F.D. Brooks, A. Buffler, V. Dangendorf, H. Friedrich, S. Guldbakke, H. Klein, J.-P. Meulders, et al., Radiation Protection Dosimetry 110 (1–4) (2004) 97.
[22] M. Nakhostin, P.M. Walker, Nuclear Instruments and Methods in Physics Research Section A 621 (1) (2010) 498.
[23] P.A. Soderstrom, J. Nyberg, R. Wolters, Nuclear Instruments and Methods in Physics Research Section A 594 (1) (2008) 79.
[24] E. Gatti, F. De Martini, Nuclear Electronics, vol. 2, IAEA, Vienna, p. 265.
[25] R. Preston, J.E. Eberhardt, R. Bencardino, J. Tickner, Software-based digital pulse processing for silicon photomultiplier radiation detectors, in: Nuclear Science Symposium and Medical Imaging Conference (NSS/MIC), IEEE, 2012, p. 462, ⟨http://ieeexplore.ieee.org/xpls/abs_all.jsp?arnumber=6551149⟩.
[26] F.D. Brooks, A. Buffler, M.S. Allie, M.S. Herbert, M.R. Nchodu, D.T.L. Jones, F.D. Smit, R. Nolte, V. Dangendorf, Radiation Protection Dosimetry 126 (1–4) (2007) 218.